SUPPLEMENTARY INFORMATION

A Bioinspired Water Oxidation Catalyst that is ~1/10th as Active as the Photosystem II Oxygen Evolving Center at pH 7: A Study of Activity and Stability Factors

Danijel Boskovic,[a] Richard Terrett,[b] Matthew Longhurst,[a] Sabeel Basheer,[a,b,c,d] Alireza Ariafard,[b] Pawel Wagner,[a] Ronald J. Pace,[b, ‡] Rob Stranger,[*,b] Gerhard F. Swiegers[*,a]

[a] Intelligent Polymer Research Institute and ARC Centre of Excellence in Electromaterials Science, University of Wollongong, Wollongong, NSW 2522, Australia

[b] Research School of Chemistry, Australian National University, Canberra, Australian Capital Territory 0200, Australia

[c] National Institute of Technology, Trichy, India 620015. Current address: VIT AP University, Andhra Pradesh, India 522237

[d] Australian Government Endeavour Research Fellow

‡ This communication is dedicated to the memory of Professor Pace (1946–2021), a colleague and veteran of Photosystem II research who passed away in January 2021

* E-mails: Rob.Stranger@anu.edu.au; swiegers@uow.edu.au

Section S1

Preparation of the electrodes

Liquid-crystalline graphene oxide (LCGO) dispersed in water (1.1 wt%, 5–10 μm flake size) was prepared by the Australian National Fabrication Facility (ANNF) Materials Node at the University of Wollongong. Phosphinic acid (50% w/w, 1 mL) was combined with 10 mL LCGO solution, effecting partial reduction to liquid crystalline reduced graphene oxide (LCrGO) (**1**). The mixture was then coated onto PET sheets (Multapex, 10 cm×10 cm×75 μm) at room temperature *via* doctor blade (0.6 mm clearance). The resulting wet brown–black films were dried in air at room temperature for 2 h and then left to dry in an oven at 80 °C overnight, washed to remove excess phosphinic acid, and thereafter thoroughly dried in air. Flexible films of LCrGO on PET (LCrGO/PET) (**2**) were obtained (black, metallic lustre). These exhibited an average thickness of 1.5±0.3 μm, conductivities of 225±56 $S \cdot cm^{-1}$ and sheet resistances of 40±10 $\Omega \cdot square^{-1}$. The latter compared well with commercially-supplied indium tin oxide (ITO) glass, which exhibit sheet resistances of 7–50 $\Omega \cdot square^{-1}$. LCrGO/PET samples were carefully cut into rectangular sections having dimensions *ca.* 2.0×2.5 cm.

Ca-doped LCrGO (**3**) was prepared by two different methods: **Method 1)** the addition of 0.2 mL 1 $mol \cdot L^{-1}$ $CaCl_{2(aq)}$ solution to 10 mL of the aforementioned LCGO dispersion, producing a viscous dispersion which was gently mixed for 20 min. Reduction with phosphinic acid and doctor blade coating onto PET sheets (Multapex) was performed analogously to the undoped LCrGO previously described, obtaining flexible Ca–LCrGO/PET films (**3b**) (black, metallic lustre) with very similar physical properties to **2**. **Method 2)** Submersion of LCrGO/PET sheets (**2**) in 1 $mol \cdot L^{-1}$ $CaCl_{2(aq)}$ solution overnight, followed by rinsing in water and air-drying obtaining **3a**.

Prepared films of **2**, **3a**, and **3b** were carefully cut into rectangular sections of approximate dimensions 2.0×2.5 cm for mounting in electrode assemblies, for subsequent electrodeposition and electrochemical experiments. Electrodeposition of MnO_x was achieved by attachment of a bare copper wire to each coated PET sheet *via* silver paste to obtain an electrical contact. The exposed copper and silver surfaces of the contact were sealed against electrolyte ingress with epoxy glue. Electrodeposition was performed according to literature procedure.[29] MnO_x electrolysis solution was prepared *via* reaction of 20 mL 1 $mol \cdot L^{-1}$ $NaNO_{3(aq)}$ solution with 10 mmol $Mn^{II}(CH_3COO)_2 \cdot 4H_2O_{(aq)}$. Electrodeposition was performed using custom-built small-volume cells described in more detail below. A superposed layer of MnO_x was electrochemically coated on each electrode at a constant current density of 200 $\mu A \cdot cm^{-2}$ for 2.5, 5, or 10 minutes. Thereafter, each electrode was rinsed by dipping in water and gently dried in N_2 gas, obtaining corresponding MnO_x/LCrGO/PET (**4**) and MnO_x/Ca–LCrGO/PET electrodes (**5a**, **5b**), respectively.

Pt-PET control electrodes (**6**) were fabricated by sputter coating a PET sheet with Pt (100 nm thickness). This sheet was then cut into 2.0×2.5 cm rectangular sections and mounted with a copper wire contact similarly to previously described electrodes. MnO_x/FTO (fluorinated tin oxide) glass control electrodes (**7**) were prepared analogously to MnO_x/LCrGO/PET electrodes, with the LCrGO/PET deposition substrate replaced with FTO glass.[16] Deposition of MnO_x was performed for 10 min at a galvanostatic current density of 200 $\mu A \cdot cm^{-2}$.

Electrochemical testing

Electrochemical experiments were carried out using a 0.1 $mol \cdot L^{-1}$ $Na_2SO_{4(aq)}$ electrolyte, with the pH adjusted to 7, on a ER466 potentiostat (eDAQ). All measurements were conducted at 21 °C, using a Pt mesh counter electrode with an electrochemical area

around 10-fold that of the working electrode. The location of the working electrode, counter electrode and reference electrode within the test cell was maintained invariant for each test. Each half cell was degassed with nitrogen and then sealed, prior to testing. Linear sweep voltammetry (LSV) was performed at a scan rate of 5 $mV \cdot s^{-1}$ over a range of 0.0–1.6 V *vs* Ag/AgCl (0.23–1.83 V *vs* standard hydrogen electrode (SHE)). Chronoamperometry was performed at 1.15 V and 1.30 V *vs* Ag/AgCl (1.38 V and 1.63 V *vs* SHE). The three-electrode cell used for electrochemical experiments on all prepared electrodes is described in detail below. During the 60 min of the chronometric measurement in Figure 3CA, the number of turnovers of the MnOx/Ca-LCrGO/PET electrode exceeded 4.5×10^{18}.

Data processing and visualisation was performed using the Numpy,[22] SciPy,[23] Pandas,[24] and Matplotlib[25] libraries for the Python programming language.

Section S2

Electrodeposition vessels used in study

Electrodeposition of MnO_x catalysts used in the present study was achieved by means of two bespoke electrochemical reactors and depicted in schematic exploded and integrated forms—as well as photographically—in Figure S1. These reactor designs were first described in Ref. [1] and are denoted EV1 and EV2 in that text. Each reactor is constructed principally from laser-cut acrylic sheets (poly(methyl methacrylate)) which were chemically welded by CH_3Cl. EV1 is a small (≈450 µL volume) vessel with no headspace, where one of the sides of the vessel is constituted by the working fluorinated tin oxide-glass (FTO-glass) electrode, which is bonded to the assembly with silicone glue. Ports drilled into the frame of EV1 permit the insertion of electrolyte as well as the counter- and reference electrodes. EV2 is a larger unsealed reactor of simple construction, in which coplanar electrodes are immersed in an electrolyte volume of up to approximately 12.4 mL.

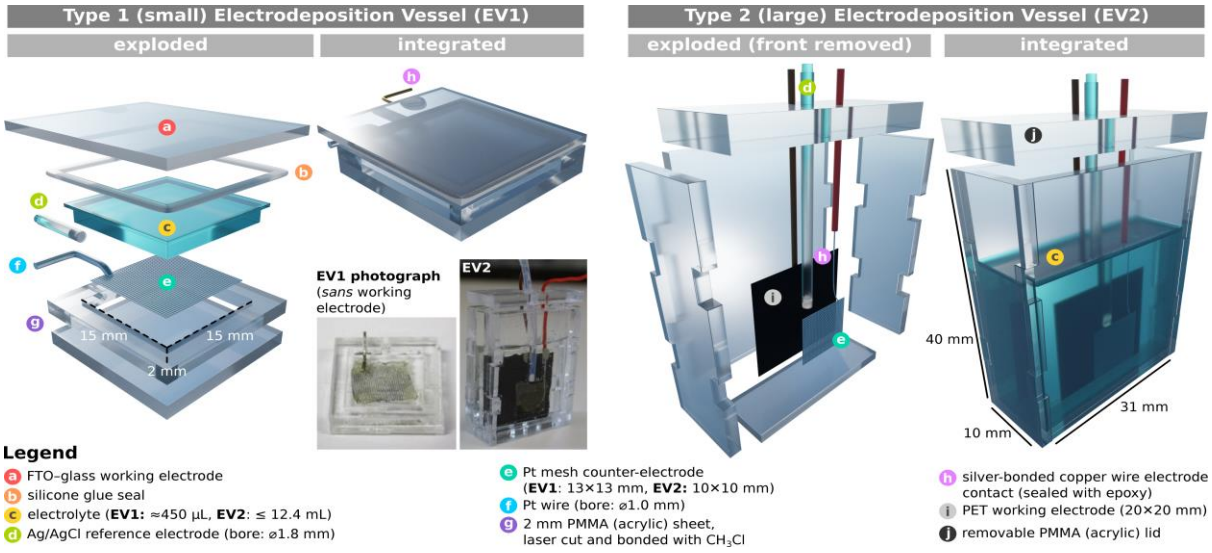

Figure S1. Schematic depiction of the electrodeposition vessels EV1 and EV2 used for preparing water oxidation electrodes used in the present study.

Section S3

Electrochemical reactor used in this study

A schematic and photographic depiction of the H-cell electrochemical reactor used in the present work is given in Figure S2.

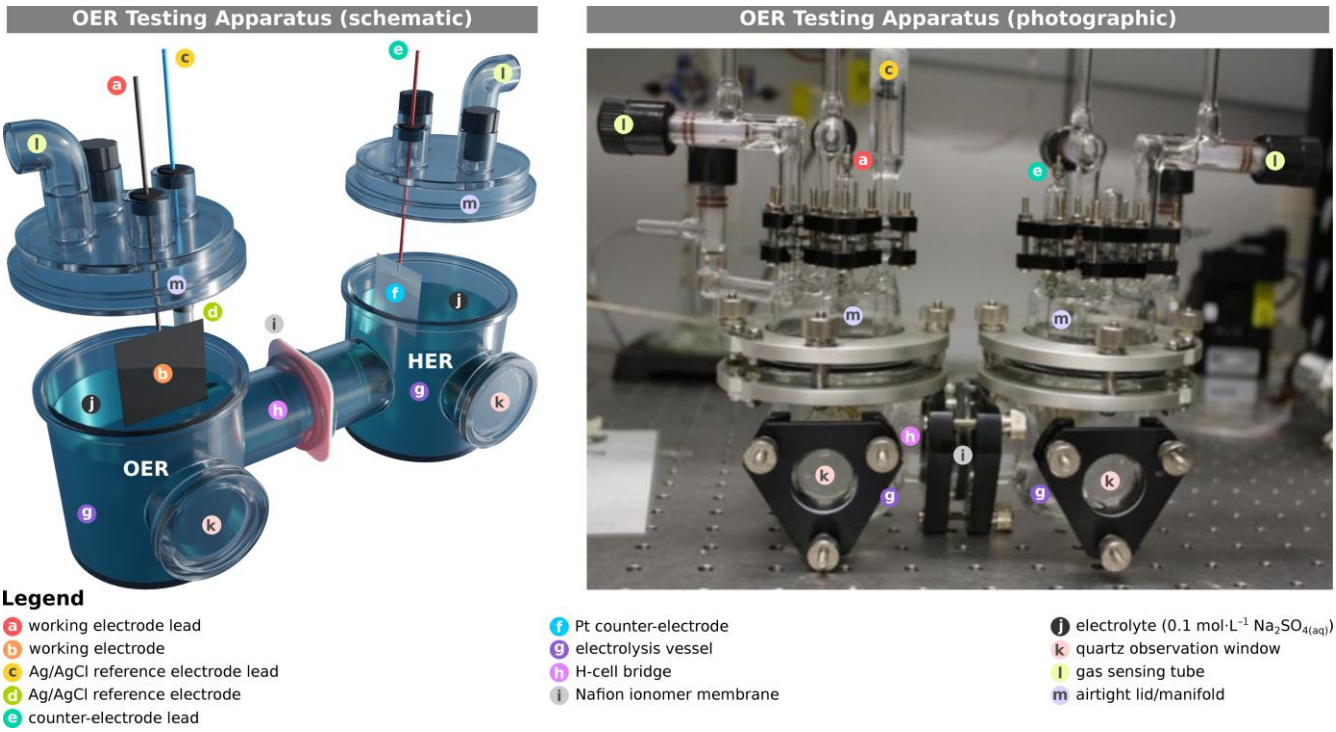

Figure S2. Schematic (left) and photographic (right) depictions of electrochemical cell used for Chronoamperometric measurements of working electrodes.

Section S4

Comparisons of catalytic activity in this work

In this work we have, essentially, sought to compare the catalytic activity of a bio-inspired, heterogenous catalyst that is on the surface of an electrode, with that of the PSII-OEC, which is an enzymatic catalyst. In Nature, all PSII-OEC catalytic sites appear to employ the same structural arrangement and the same catalytic mechanism. Their catalytic activity is therefore best described in terms of their 'turnover frequency', which is generally a replicable quantity under comparable conditions, when examining different samples of such a catalyst. However, it is very much more complex to accurately determine a turnover frequency for each type of site in a surface heterogeneous catalyst. Such turnover frequencies are generally also not comparable to the turnover frequency of the PSII-OEC since many different catalytic sites are typically present, each with a different 3D environment. The different sites may have very different turnover frequencies. For example, a catalytic site may be on an edge, a face, or in a defect on the surface of a heterogeneous catalyst. A key challenge in assessing the catalytic performance of bio-inspired heterogeneous catalysts on an electrode surface is therefore to develop a means to make a comparison with the equivalent enzymatic catalyst.

In this work, we have noted that, despite the profound differences, there is, nevertheless, one point of similarity in the bioinspired and PSII-OEC systems. The catalytic rate of the PSII-OEC is dependent on the rate of electron transfer between the Y_z tyrosine (which forms part of a larger organic structure) and the catalytically active Mn_4CaO_5 cluster. Similarly, the catalytic rate of the bio-inspired catalyst is dependent on the rate of electron transfer between an organic structure (namely, the liquid-crystalline reduced graphene oxide layer) and the active Mn oxo and Ca ions in the adjacent layer.

Accordingly, we have measured the currents (i.e. the rates of electron transfer) produced

by the bio-inspired heterogeneous catalyst surface in its different forms, and compared them with those expected for a closely-packed monolayer of OEC cofactors, operating as if they were in the PSII-OEC, and having the optimum site density of 10^{14} sites/cm^2 (corresponding to an OEC footprint of 1 nm^2). That is, we have made a comparison of the catalytic activity *per unit area* of coverage of the bioinspired catalyst vs. the OEC. We have not made a comparison of the *intrinsic* catalytic activity of the bioinspired catalyst and the OEC.

Developing a heterogeneous catalyst with comparable performance to the PSII-OEC at pH 7 offers fundamental as well as potential commercial-industrial advances in the future.

Use of unbuffered electrolyte

The results reported here were obtained without a traditional buffer species in the electrolyte (although studies with a traditional buffer [8] produced very similar results to those shown here). This was intended to provide the most authentic possible comparison with the PSII-OEC and avoid artefacts associated with the use of buffers. Traditional buffer species have previously been shown, for example, to directly participate in surface reactions [9] and to set the catalytic rate according to their rate of mass transport [10].

The above observations suggest, also, that a buffering species may already be present in our system. Alternatively, or additionally, the pHs of the two half cells may have equilibrated rapidly, this process being presumably accelerated by: (i) the small gap between the electrodes, (ii) the relatively large volume of electrolyte in the test cell, (iii) the tiny currents involved, and (iv) ready proton exchange between the half-cells. As water splitting does not involve net production of H^+/OH^- ions, every proton produced during oxygen production at the anode must necessarily be matched by a proton consumed during hydrogen production at the cathode.

The liquid crystalline (LC) reduced graphene oxide (rGO) substrate may potentially have acted to buffer the reaction at the low current densities examined. We note that even after reduction of graphene oxide, a significant number of oxygen functional groups are known to remain on rGO. Chemical species containing electron-rich heteroatoms (e.g. La_2O_3 or lutidine) have previously been shown to act as effective buffer species in water oxidation electrocatalysis in pH 7 water [11]. The presence of such non-traditional buffer species was shown to allow for steady and unchanging rates of oxygen generation at fixed voltage for at least 60 min in pH 7 aqueous solution (in the absence of a traditional buffer such as K-phosphate) [11]. Reduced graphene oxide has also been shown to act as a pH sensor that undergoes ready protonation and deprotonation reactions at moderate pH [12]. It may be used as a buffer layer in solar cells [13].

While these conclusions are still under study and will be reported elsewhere, they are consistent with the following observations in the studied system:

- The pH of the electrolyte near the working, oxygen-producing electrode was monitored during the experiments with no significant fluctuations observed. This could not be the case if there was a local buildup of protons in the oxygen-producing anode half-cell.
- Figure 3CA in the manuscript shows that, at a fixed voltage, the electrodes exhibited no or little change in current over 1 h of continuous oxygen generation. This could not have occurred if the local pH declined at the electrode surface, since such a decline would have increased the overpotential for catalytic oxygen production, sharply diminishing the current.
- The experiments generally did not demonstrate the sort of systematic and substantial declines in current that would be expected from an increase in overpotential arising from a decline in local pH. For this reason, it can be concluded that, even if there was an undetected decline in the local pH at the working electrode, this would have resulted

in the reported currents being lower than they should have been, not higher. That is, the catalytic effects reported in this work would have been smaller than they should have been, not larger.

Tafel plot comparisons

The performance of selected catalytic electrodes at pH 7 were also compared using Tafel plots. The plots are depicted overleaf. As can be seen, the iR-corrected MnO_4/Ca-LCrGO/PET electrode displayed a steeper Tafel slope than the iR-corrected Pt/PET control but had a higher exchange current density. As modelled here, the PSII-OEC had the lowest Tafel slope.

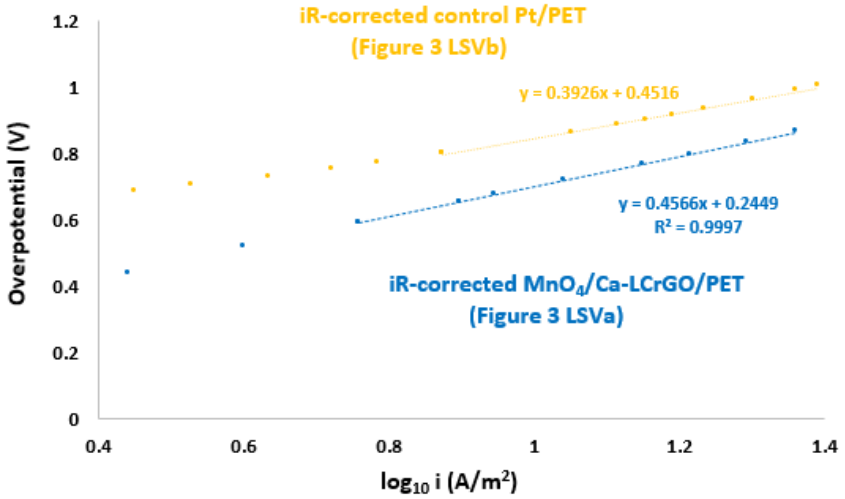

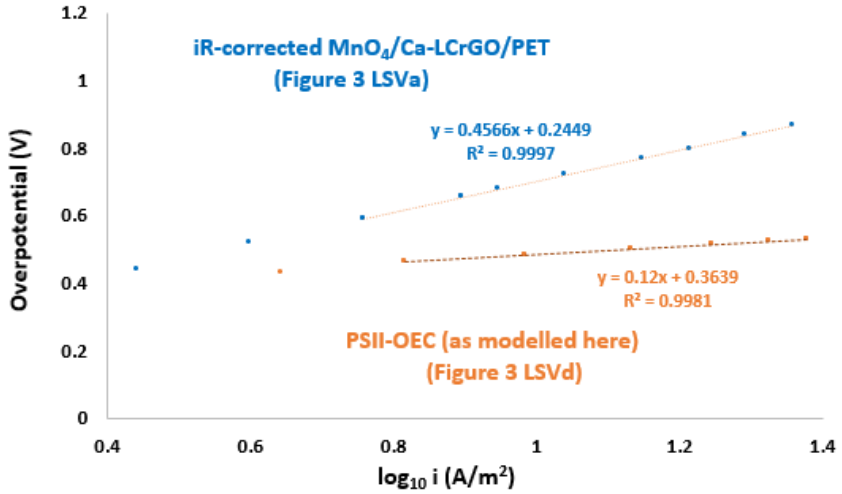

Electrode (Water oxidation catalysis)	Tafel Slope (A) (mV/decade)	Exchange current density (i_o) (A/m^2)
iR-corrected control Pt/PET	392	0.071
iR-corrected MnO_4/Ca-LCrGO/PET	457	0.291
PSII-OEC (as modelled here)	120	0.001

Section S5

iR Correction of LSV data

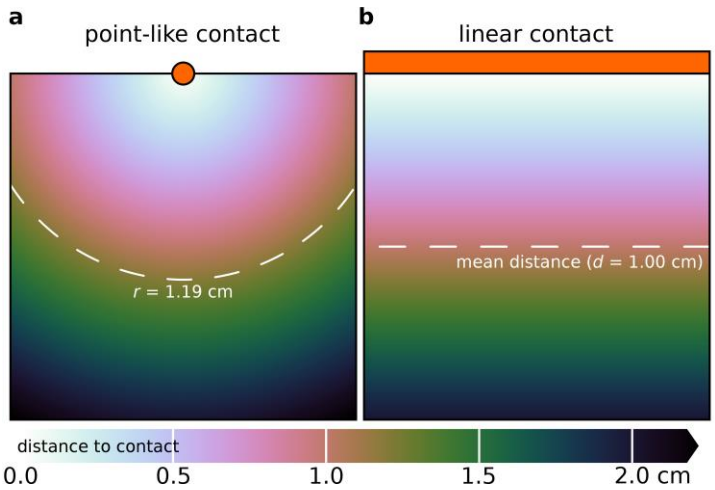

Figure S3. Illustrations of the distance function of points on a 2×2 cm active-area electrode employing **a)** two-dimensional, and **b)** one-dimensional metrics, representing point-like and linear current collector contacts, respectively.

A significant ohmic potential drop occurs in the plane of the OER electrodes prepared for the present study. This is because current collection occurs at the edge of the electrochemically active area. The PET film used as the substrate for LCrGO deposition was found to have a thickness of 1.5×10^{-6} m, with a resistivity ρ of 4.44×10^{-5} Ω·m. For a 2×2 cm electrode, a cross-sectional area A of 3×10^{-8} m^2 is obtained. The linear resistance of points on the electrode was modelled as being proportional to the distance between a point on the electrode and the current collector contact.

The mean resistance across the electrode is modelled as:

$$\bar{R} = \frac{\rho \bar{L}}{A}$$

Where $\bar{L}$ is the mean distance from the current collector. As the electrical contact for the current collector to each electrode is variable, two limiting cases for the geometry of the current collector are considered, one which considers the current collector as point-like and

situated at the midpoint of an electrode edge (the two-dimensional case, Figure S3a) and the other which considers the contact as spanning the length of one of the sides of the electrode (the one-dimensional case, Figure S3b). The resistance of the electrical contact is neglected from this model. The electrodes investigated in the present work more closely resemble the two-dimensional case due to the small size of the current collector contact with respect to the width of the electrode, however varying the aspect ratio of the electrode active area or the width of the contact interpolates between these two models.

In the one-dimensional case, $\bar{L}$ is 1.00 cm (analytic), whilst in the two-dimensional case $\bar{L}$ was found to be approximately 1.19 cm *via* a Monte Carlo calculation. These data yield bounding iR corrections of 14.8 Ω and 17.6 Ω, respectively.

The corresponding iR correction applied to the electrode voltage is:

$$V_{corr.} = V_{meas.} - I\bar{R}$$

Section S6

Programmatic onset potential estimation

To avoid subjective estimations, onset potentials for LSV data were estimated using an automated tangent approach. This approach obtains the intercept of (pseudo)tangent lines fitted to the non-Faradaic and Faradaic regions of the LSV curve for each electrode. The non-Faradaic tangent is a horizontal line fit in one parameter (the non-Faradaic current density offset, b_1), whereas the Faradaic tangent is fit in two parameters (the Faradaic current density offset b_2 and the slope m). The non-Faradaic tangent is fit to points satisfying a 'flatness condition' where $\left|\frac{dj}{dV}\right| \leq 0.05$ mA·cm^{-2}·V^{-1}, obtained numerically. Where the current density does not increase monotonically with respect to voltage (due to the presence of oxidative prefeatures in the LSV curve), only the lowest potential continuous span of the LSV curve satisfying this criterion is considered. The Faradaic region is defined as the region of the LSV for which the current density is greater than 50% of the maximum reported current density. The latter measure assumes that the high-current region of the recorded LSV curve is Faradaic in nature and quasi-linear. Therefore, R^2 values are given for each Faradaic tangent, indicating the fit quality for the corresponding region (the non-Faradaic tangent R^2 is not defined due to horizontality).

Recent scholarship has problematised popular tangent intercept and so-called *'de visu'* approaches to onset potential estimation, [7] and has proposed alternative measures based on the maxima of the second derivative of interpolated LSV data (the SODDM approach).[7] The SODDM approach was attempted on data reported in the present manuscript, however noise in the second derivatives of the data prevented this method from being used fruitfully (- this is a general feature of the higher-order derivatives of instrumental data). The use of an automated tangent approach in the present work provides a well-defined

onset potential estimate both between reported datasets and with other works. An exemplary plot of this method is given in Figure S4.

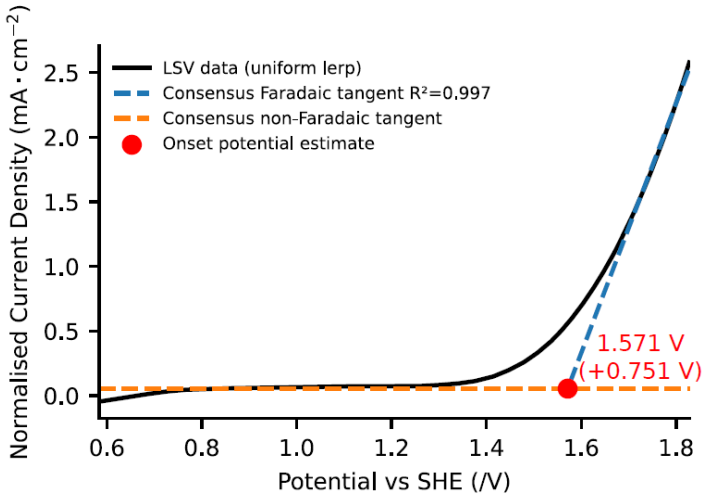

Figure S4: Exemplary plot of onset potential determination for Pt-PET control electrode, using automated approach.

Table S1. Calculated onset potentials of catalytic species prepared in the present work, versus SHE. *'Initial current'*: potential at which the current density exceeds the non-Faradaic regime by +0.05 mA·cm^{-2}. *'Tangent proj.'*: onset potential obtained by tangent projection method. *'Fit R^2'*: R^2 value for the fit of the Faradaic tangent to LSV data.

	Onset Potential (/V)			Onset Overpotential
Catalyst	Initial Current	Tangent proj.	Fit R^2	(/V)
Method 1				
Ca-LCrGO/PET **(3b)**	1.10	1.33	0.999	0.51
MnOx /Ca-LCrGO/PET **(5b)**	1.11(0)	1.34(0)	0.000	0.52
Method 2				
MnOx /Ca-LCrGO/PET **(5a)**	0.99	1.42	0.997	0.60
" iR-corrected	1.05(3)	1.42(0)	0.000	0.60
Calcium-free				
MnO_x /LCrGO/PET **(4)**	0.99	1.38	0.999	0.56
Control conditions				
LCrGO/PET **(2)**	0.97	1.38	0.999	0.56
Pt-PET **(6)**	1.37	1.57	0.997	0.75
MnOx /FTO **(7)**	1.47	1.54	0.000	0.72
PSII OEC				
Literature[5]	1.11–1.30	—	0.000	0.48
Model ($\rho = 10^{14}$ cm^{-2})	1.21	1.28	0.994	0.46
Model ($\rho = 10^{15}$ cm^{-2})	1.16	1.22	0.990	0.40

Section S7

Supporting chronoamperometry data

Supporting chronoamperometry data for catalysts and control conditions are illustrated in Figure S5. Electrolysis of electrode **5a** at 1.83 V was accompanied by visible degradation of LCrGO, however this was not characterised in detail.

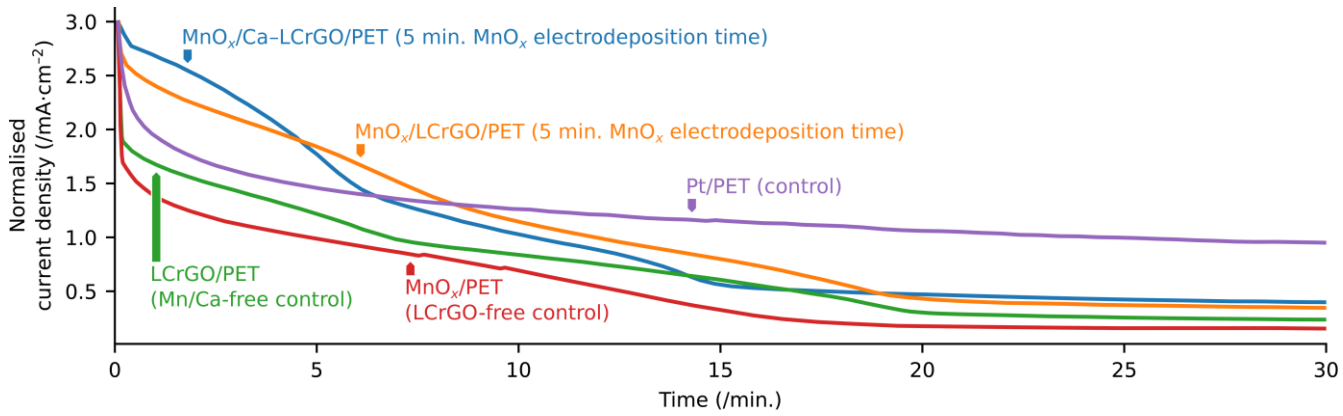

Figure S5: **Supporting** chronoamperometry data for prepared catalytic electrodes (Method 2) and controls at a potential of 1.6 V versus an Ag/AgCl reference electrode in a 0.1 mol·L^{-1} $Na_2SO_{4(aq.)}$ solution.

Section S8

Modelling of PSII-OEC voltammogram

The OEC turnover frequency can be estimated *via* the electron paramagnetic resonance (EPR) lifetime of the Tyrosine Z (D1-Tyr$_{161}$) radical in the S_3 state. A half-life for this state of $t_{\frac{1}{2}} \approx 1$ ms was obtained by Razeghifard and Pace, and this data is reproduced in Figure S6a. [2] As the $S_3 \rightarrow S_4$ transition is rate-limiting, this half-life constrains the total turnover frequency of the OEC. [4, 5] Considering a hypothetical planar non-porous electrode coated with functional OEC cofactors with an areal density of 1×10^{14} cm^{-2} (corresponding to an OEC footprint area of 1 nm^2), an effective electrode current density of 8 mA·cm^{-2} is obtained.

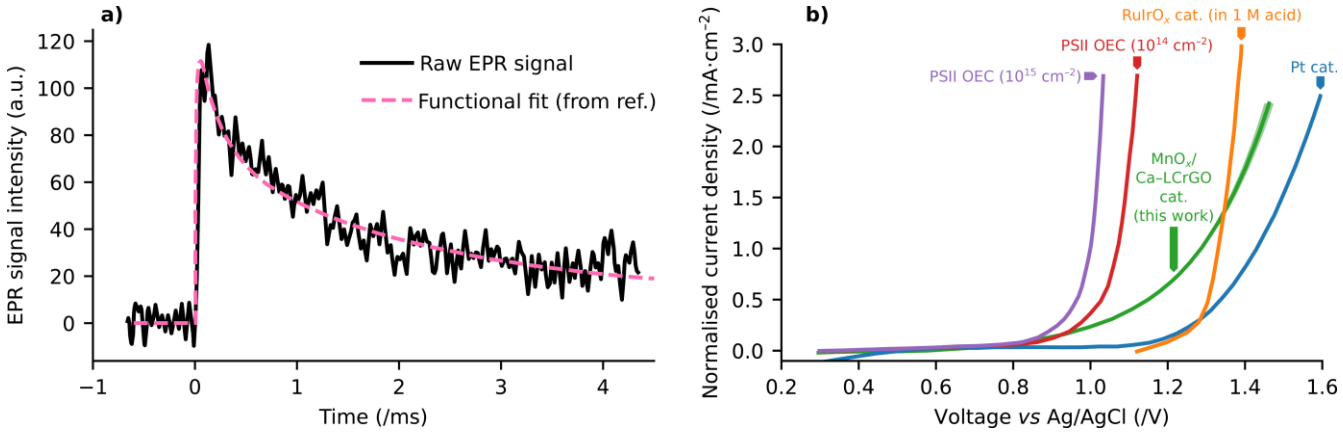

Figure S6. a) Decay of PSII-OEC Tyrosine Z (D1-Tyr$_{161}$) radical during rate-limiting $S_3 \rightarrow S_4$ transition of the OEC, establishing a $t_{\frac{1}{2}}$ for this transition of approximately 1 ms. Data reproduced from Ref. [2].
b) Experimental RuIrO$_x$, (Mamaca, et al.) Pt-PET, MnO$_x$/Ca-LCrGO/PET (present work), and PSII OEC model LSV curves. Data reproduced from Ref. [3].

The voltammogrammetric behaviour of a catalyst at the anode surface depends on two factors: a) the activation energy necessary to allow incipient O–O bond formation (reflected in the catalytic overpotential), and b) the efficiency of electron transfer to the activated site (principally a quantum tunnelling process). The former factor informs the point on the LSV

where the current density becomes non-zero, and the latter informs the quasi-linear limiting slope of the *I*/*V* relation at high currents. The LSV performance of the PSII OEC is estimated by observing that the distal oxidant of the OEC is the P_{680}/P_{680}^{+} couple, which has a midpoint oxidation potential of approximately 1.3 V at neutral pH, [5] or approximately 1.1 V *versus* an Ag/AgCl reference electrode. At present, no synthetic water oxidation catalyst meets or exceeds the performance envelope of the PSII OEC, however LSV data for some illustrative catalysts are depicted in Figure S6b. The $RuIrO_x$ catalyst of Mamaca, *et al.* [3] exhibits a very steep current density/potential relation (≈100 $mA \cdot cm^{-2}V^{-1}$) and has been selected as a prototype for OEC-like performance. The LSV data corresponding to this catalyst was obtained in 1 $mol \cdot L^{-1}$ $H_2SO_{4(aq)}$ solution. The effective operational pH of the OEC is not well-defined, but has been established as $\gtrapprox$ 5, as this value is the apparent lower bound on the pKa for OEC function (based on *in vivo* chloroplastic studies by Bernát, *et al.* [6]). This value corresponds to a potential shift of approximately −300 mV, which is applied to the $RuIrO_x$ LSV data of Mamaca, *et al.* to obtain a notional OEC LSV model. This model obtains a current density of 4 $mA \cdot cm^{-2}$ to 8 $mA \cdot cm^{-2}$ at a potential of 1.1 V *versus* a Ag/AgCl reference electrode, which is comparable to the OEC under similar driving conditions. Therefore, within the approximations attending this estimate, we take this derived LSV curve as representative of OEC performance at an active site density of 1×10^{14} cm^{-2}. The 1×10^{15} cm^{-2} site density estimate is obtained by multiplying the current density of the 1×10^{14} cm^{-2} site density condition by a factor of 10.

References (Supporting Information only)

[1] Boskovic, D. Studies of manganese porphyrin-PEDOT and manganese oxide-graphene composites as water oxidation electrocatalysts and photocatalysts. PhD thesis. University of Wollongong, New South Wales, Australia, 2016, pp. 66–68.

[2] Razeghifard, M. R.; Pace, R. J. Electron paramagnetic resonance kinetic studies of the *S* states in spinach PSII membranes. *Biochimica et Biophysica Acta (BBA) - Bioenergetics* **1997**, *1322.2-3*, 141–150.

[3] Mamaca, N.; Mayousse, E.; Arrii-Clacens, S.; Napporn, T.; Servat, K.; Guillet, N.; Kokoh. K. Electrochemical activity of ruthenium and iridium based catalysts for oxygen evolution reaction. *Applied Catalysis B Environmental*, **2012,** 111-112, 76–380.

[4] Vos, M. H.; van Gorkom, H. J.; van Leeuwen, P. J. An electroluminescence study of stabilization reactions in the oxygen-evolving complex of Photosystem II. *Biochimica et Biophysica Acta (BBA) - Bioenergetics* **1991**, *1056.1*, 27–39.

[5] Rappaport, F.; Diner, B. Primary photochemistry and energetics leading to the oxidation of the $(Mn)_4Ca$ cluster and to the evolution of molecular oxygen in Photosystem II. *Coordination Chemistry Reviews* **2008**, *252.3–4*, 259–272. See also: Ishikita, H.; Loll, B.; Biesiadka, J.; Saenger, W.; Knapp, E.-W. Redox Potentials of Chlorophylls in the Photosystem II Reaction Center. *Biochemistry* **2005**, *44*, 4118–4124.

[6] Bernát, G.; Morvadi, F.; Feyziyev, Y.; Styring, S. pH Dependence of the Four Individual Transitions in the Catalytic S-Cycle during Photosynthetic Oxygen Evolution. *Biochemistry* **2008**, 41.18, 5830–5843. .

[7] de Falco, G.; Florent, M.; De Rosa, A.; Bandosz, T. J. Proposing an unbiased oxygen reduction reaction onset potential determination by using a Savitzky-Golay differentiation procedure. *J. Colloid Interface Sci.* **2021**, *586*, 597–600.

[8] Naito, T.; Shinagawa, T.; Nishimimoto, T.; Takanabe, K. Water Electrolysis in Saturated Phosphate Buffer. *ChemSusChem* **2020**, *13*, 5921–5933.

[9] Shinagawa, T.; Obata, K.; Takanabe, K. Switching of Kinetically Relevant Reactants for the Aqueous Cathodic Process Determined by Mass-transport Coupled with Protolysis. *ChemCatChem* **2019**, *11*, 5961–5968.

[10] Shinagawa, T.; Takanabe, K. Electrocatalytic Hydrogen Evolution under Densely Buffered Neutral pH Conditions. *J. Phys. Chem. C* **2015**, *119*, 20453–20458.

[11] Takashima, T.; Ishikawa, K.; Irie, H. Induction of Concerted Proton-Coupled Electron Transfer during Oxygen Evolution on Hematite Using Lanthanum Oxide as a Solid Proton Acceptor. *ACS Catalysis* **2019**, *9*, 9212-9215. Figure S6 demonstrates sustained (60 min), near-constant catalytic currents for water oxidation, at a fixed voltage, in the presence of non-traditional buffering species containing electron-rich heteroatoms.

[12] Chinnathambi, S.; Euverink, G. J. W. Hydrothermally reduced graphene oxide as a sensing material for electrically transduced pH sensors. *J. Electroanal. Chem.* **2021**, *895*, 115530.

[13] See, for example: Antink, W. H.; Choi, Y.; Seong, K.-D.; Kim, J. M.; Piao, Y. Recent Progress in Porous Graphene and Reduced Graphene Oxide-Based Nanomaterials for Electrochemical Energy Storage Devices. *Adv. Mater. Interfaces* **2018**, *5*, 1701212.